Mechanical Control of Nonlinearity in Doubly Clamped MEMS Beam Resonators Using Preloaded Lattice-Mismatch Strain

Chao Li, Boqi Qiu, Yuri Yoshioka, Kazuhiko Hirakawa, and Ya Zhang

Phys. Rev. Applied **19**, 024025 — Published 9 February 2023

DOI: 10.1103/PhysRevApplied.19.024025

Mechanical control of nonlinearity in doubly clamped MEMS beam resonators using preloaded lattice-mismatch strain

Chao Li[1a)], Boqi Qiu[2a)], Yuri Yoshioka[1], Kazuhiko Hirakawa[2,3b)], and Ya Zhang[1c)]

[1]*Institute of Engineering, Tokyo University of Agriculture and Technology, Koganei-shi, Tokyo, 184-8588, Japan*

[2]*Institute of Industrial Science, University of Tokyo, 4-6-1 Komaba, Meguro-ku, Tokyo 153-8505, Japan*

[3]*Institute for Nano Quantum Information Electronics, University of Tokyo, 4-6-1 Komaba, Meguro-ku, Tokyo 153-8505, Japan*

We have theoretically clarified the mechanism of strain tuning effect on the control of mechanical nonlinearity in doubly clamped MESM beam resonators, and experimentally demonstrated that the nonlinearity can be effectively suppressed with a preloaded lattice-mismatch strain in the MEMS beam. The mechanical nonlinearity arises from the hardening and softening nonlinearity terms in the Duffing motion equation of the MEMS beam. By approaching the buckling condition of the MEMS beam, the substantially increased softening nonlinearity greatly compensates for the hardening nonlinearity, resulting in the suppression of the total nonlinearity. Utilizing this knowledge, we fabricated $In_xGa_{1-x}As$ MEMS beams with a preloaded lattice-mismatch strain, which was achieved by adding a small amount (x =~0.4%) of indium to the GaAs MEMS beam in the wafer growth. The buckling condition in the experiment was achieved by carefully modulating the length of $In_xGa_{1-x}As$ MEMS beams. As a result, the mechanical nonlinearity is largely modulated from hardening to softening and reaches a quasi-zero value near the buckling condition, demonstrating the effectiveness of using lattice mismatch for controlling the mechanical nonlinearity of MEMS resonators.

---

a) Chao Li and Boqi Qiu contributed equally to this paper.

b) Electronic mail: hirakawa@iis.u-tokyo.ac.jp

c) Electronic mail: zhangya@go.tuat.ac.jp

Introduction

Microelectromechanical system (MEMS) resonators [1-3] are promising candidates for high-sensitivity sensing applications. MEMS resonators can detect small shifts in the resonance frequency owing to the high quality (Q)-factors. This property has been utilized for the detection of mass [4-6], spin orientation [7], charge [8-10] , temperature [11,12] , and infrared radiation [13,14]. Previously, we reported using a doubly clamped MEMS beam resonator as a fast and sensitive bolometer for terahertz (THz) detection [15,16]. The MEMS beam is heated up owing to the absorption of THz electromagnetic waves, and the induced thermal strain shifts the resonance frequency of the MEMS resonator. In sensing applications with MEMS resonators, a large linear oscillation amplitude is generally preferable to reduce the frequency noise and improve the signal-to-noise ratio [17], which can be achieved by increasing the driving force. However, with increasing oscillation amplitude, the MEMS resonators commonly enter the nonlinear oscillation region because of the mechanical nonlinearity, where hysteretic oscillations and increased frequency noise have been observed [18,19]. The control of mechanical nonlinearity is therefore desirable for achieving the low-noise operation of MEMS resonators.

Recently, we reported on controlling the mechanical nonlinearity of MEMS beam resonators through a thermal strain tuning effect [20]. We observed a significant reduction in the mechanical nonlinearity near the buckling point of the MEMS beam. However, the origin of such thermal strain tuning on the mechanical nonlinearity has not yet been theoretically clarified. Moreover, controlling the nonlinearity by the thermal effect requires additional heating to the MEMS beam, which increases the noise and frequency drift coming from the thermal effect. The thermal strain is not the only method to buckle the MEMS beam. It has been reported that the buckling condition of the MEMS beam can be precisely controlled by preloading a lattice-mismatch strain [21], which can be achieved in the wafer growth stage without the requirement of additional heating. Therefore, the use of a lattice mismatch would be a promising approach to control the mechanical nonlinearity of the MEMS beam resonators.

In this work, we clarify the mechanism of strain tuning effect on the control of mechanical nonlinearity in doubly clamped MESM beam resonators, and then demonstrate that the nonlinearity can be effectively suppressed with a preloaded lattice-mismatch strain in the MEMS beam. The nonlinearity of the MEMS beam arises from the cubic (hardening) and quadratic (softening) nonlinearity terms in the Duffing motion equation. With strain tuning, the nonlinearity can be well suppressed when approaching the buckling condition of the MEMS beam. This is because the steep increase in the softening nonlinearity near the buckling condition greatly compensates for the hardening nonlinearity, resulting in the suppression of the total nonlinearity. Utilizing this knowledge, we fabricated $In_xGa_{1-x}As$ MEMS beams with a preloaded lattice-mismatch strain, which was achieved by adding a small amount (x =~0.4%) of indium to the GaAs MEMS beam in the wafer growth. The buckling condition in the experiment was achieved by carefully modulating the length of $In_xGa_{1-x}As$ MEMS beams. We estimated the total nonlinearity in the MEMS beam by measuring its resonance frequency shift as a function of oscillation amplitude. As a result, the nonlinearity is largely modulated from hardening to softening as L increases and reaches a quasi-zero value near the buckling condition, demonstrating the effectiveness of using lattice mismatch for controlling the mechanical nonlinearity of MEMS resonators. Furthermore, we have introduced the effective nonlinearity, $Y_{(\alpha,\beta)}$, to reproduce the total nonlinearity in the MEMS beam, which intuitively show the effect of hardening and softening nonlinearities on the total nonlinearity, allowing one can understand the origin of the nonlinearity change.

Equation of Motion

The Duffing equation with quadratic and cubic nonlinearities is commonly utilized for studying the nonlinear resonance behavior of MEMS resonators [22-26]. For an initially straight doubly clamped MEMS beam resonator with length L, the motion equation of its transverse vibrations is approximately described by the Euler–Bernoulli equation as [23]

$$\rho S \frac{\partial^2 X}{\partial t^2} = -EI \frac{\partial^4 X}{\partial u^4} + T \frac{\partial^2 X}{\partial u^2} \tag{1}$$

with the following boundary conditions:

$$X|_{u=0,L} = 0 \text{ and } \left.\frac{\partial X}{\partial u}\right|_{u=0,L} = 0, \tag{2}$$

where *X(u,t)* is the transverse displacement from the equilibrium; *u* is the coordinate along the length of the beam; *t* is the time scale; *ρ* is the density; *E* is the Young's modulus; *L* is the beam length; *S* and *I* denote the cross-section area and the moment of inertia ($S=bh$ and $I=bh^3/12$ for beams of rectangular cross-sections, with *b* and *h* being the width and thickness of the MEMS beam, respectively); *T* is the tension in the MEMS beam, which is composed of its inherent tension T_0 (positive for a tensile force and negative for a compressive force) and the additional tension ΔT coming from the extension of the beam length (ΔL) in the vibration.

Here, we only consider the first bending mode of the MEMS beam, where the mechanical nonlinearity is affected by the internal strain the most. We assume that the transverse displacement of the MEMS beam can be expressed as the product of the mode profile function $\phi(u)$ and the central displacement of the beam $x(t)$ as

$$X(u,t) = \phi(u)x(t) \tag{3}$$

Then, we can obtain a duffing equation of motion for the MEMS beam as [23]

$$\ddot{x} + \left[\frac{EI}{\rho S}\frac{\int(\phi^{uu})^2 du}{\int \phi^2 du} + \frac{T_0}{\rho S}\frac{\int(\phi^{u})^2 du}{\phi^2 \int du}\right] x + \left[\frac{E}{2\rho L}\frac{\left(\int(\phi^{u})^2 du\right)^2}{\int \phi^2 du}\right] x^3 = 0, \tag{4}$$

where $\phi^u = \frac{\partial \phi}{\partial u}$, and $\phi^{uu} = \frac{\partial^2 \phi}{\partial u^2}$. As seen in Eq. (4), the cubic nonlinearity coefficient $\alpha = \frac{E}{2\rho L}\frac{\left(\int(\phi^{u})^2 du\right)^2}{\int \phi^2 du} > 0$, which gives a hardening nonlinearity [22,27].

Next, we consider a MEMS beam with an initial center deflection x_0. When a compressive strain ε is introduced in the beam, the center deflection increases to x_T, as schematically shown in Fig. 1 (a). The steady-state equation under this condition is expressed as

$$EI(x_\mathrm{T}-x_0)\int(\phi^{uu})^2du+T_0x_\mathrm{T}\int(\phi^u)^2du=0, \tag{5}$$

from which we can derive x_T as a function of the initial center deflection x_0 and the inherent tension T_0:

$$x_\mathrm{T}=\frac{EI\int(\phi^{uu})^2du}{EI\int(\phi^{uu})^2du+T_0\int(\phi^u)^2du}x_0. \tag{6}$$

Here, the inherent tension $T_0=ES\varepsilon_\mathrm{r}$ is different from the induced compressive load $T=ES\varepsilon$, since part of the compressive strain, ε, is released by the center deflection increase. The residual strain ε_r is expressed as

$$\varepsilon_\mathrm{r}=\varepsilon-\frac{({x_\mathrm{T}}^2-{x_0}^2)}{2L}\int(\phi^u)^2du. \tag{7}$$

The beam length extends when it differs from its equilibrium position in the oscillation with an additional displacement x as

$$\Delta L=\frac{(x+x_\mathrm{T})^2-{x_\mathrm{T}}^2}{2}\int_0^L du\left(\frac{\partial\phi}{\partial u}\right)^2=\frac{x^2+2x_\mathrm{T}x}{2}\int_0^L du\left(\frac{\partial\phi}{\partial u}\right)^2, \tag{8}$$

ΔL gives an additional tension $\Delta T=ES\Delta L/L$ to the MEMS beam. With the total tension $T=T_0+\Delta T$, the motion equation of the MEMS beam becomes

$$\ddot{x}+\left[\frac{EI}{\rho S}\frac{\int(\phi^{uu})^2du}{\int\phi^2du}+\frac{T_0}{\rho S}\frac{\int(\phi^u)^2du}{\int\phi^2du}+x_\mathrm{T}^2\frac{E}{\rho L}\frac{\left(\int(\phi^u)^2du\right)^2}{\int\phi^2du}\right]x+\left[\frac{E}{2\rho L}\frac{\left(\int(\phi^u)^2du\right)^2}{\int\phi^2du}\right]x^3+$$

$$\left[\frac{3x_{\mathrm{T}}E}{2\rho L}\frac{\left(\int(\phi^{u})^{2}du\right)^{2}}{\int\phi^{2}du}\right]x^{2}=0. \tag{9}$$

Compared with Eq. (4), by considering an initial center deflection, an additional quadratic nonlinear term $\beta=\frac{3x_{\mathrm{T}}E}{2\rho L}\frac{\left(\int(\phi^{u})^{2}du\right)^{2}}{\int\phi^{2}du}=3x_{\mathrm{T}}\alpha$ arises. As we have discussed in a previous publication [20], the quadratic nonlinear term always gives a softening nonlinearity to the MEMS resonator, which compensates for the cubic hardening nonlinearity and leads to the suppression of the total nonlinearity. Furthermore, the quadratic term is proportional to the center deflection x_{T}, indicating that the nonlinearity can be suppressed by precisely controlling x_{T}.

From Eq. (9), we can see that both the resonance frequency and nonlinearity terms are affected by the mode shape $\phi(u)$. For the first bending mode of a curved MEMS beam, $\phi(u)$ is usually approximated by [28]

$$\phi(u)=\frac{1}{2}(1-\cos\frac{2\pi}{L}u). \tag{10}$$

By substituting Eq. (10) to Eq. (9), we can express the resonance frequency ω_0^2 and nonlinearity terms as

$$\omega_0^2=\frac{EI}{\rho S}\frac{16\pi^4}{3L^4}+\frac{T_0}{\rho S}\frac{4\pi^2}{3L^2}+x_{\mathrm{T}}^2\frac{E}{\rho}\frac{2\pi^4}{3L^4},$$

$$\alpha=\frac{E\pi^4}{3\rho L^4}, \tag{11}$$

$$\beta=\frac{E\pi^4}{\rho L^4}x_{\mathrm{T}}=3x_{\mathrm{T}}\alpha.$$

By using Eq. (10), Eqs. (6), (7) can also be simplified as

$$x_{\mathrm{T}}=\frac{1}{1-\frac{\varepsilon_r}{\varepsilon_{cr}}}x_0 \tag{12}$$

and

$$\varepsilon_r = \varepsilon - ({x_{\mathrm{T}}}^2 - {x_0}^2)\frac{\pi^2}{4L^2} \tag{13}$$

Numerical analysis results

Numerical analysis is performed for the MEMS beam resonators with dimensions of 100 μm(L)×30 μm(b)×1 μm(h) and with E=85.9 GPa, ρ=5307 kg/m^3 applied for the Young's modulus and density of GaAs material. The left y-axis of Fig. 1(b) plots the normalized center deflection, x_{T}/h, as a function of the compressive strain, $\varepsilon/\varepsilon_{\mathrm{cr}}$, calculated for various initial center deflections, x_0/h. Here, $\varepsilon_{\mathrm{cr}} = \frac{\pi^2}{3}\frac{h^2}{L^2}$ is Euler's buckling critical strain of the MEMS beam. As seen, in the case of x_0=0, the center deflection, x_{T}, remains zero before buckling ($\varepsilon/\varepsilon_{\mathrm{cr}}<1$), and starts to increase with the compressive strain following $x_{\mathrm{T}} = \frac{2L(\varepsilon-\varepsilon_{\mathrm{cr}})}{\pi}$ after buckling ($\varepsilon/\varepsilon_{\mathrm{cr}} \geq 1$). However, in the case of x_0>0, x_{T} is given by the initial deflection, x_0, as well as the compressive strain, ε, as derived from Eqs. (6) and (7). Under this condition, x_{T} increases with ε even when $\varepsilon<\varepsilon_{\mathrm{cr}}$. This can be understood by the fact that the beam with an initial center deflection tends to bend more when a compressive strain is applied. The residual strain ε_{r} in the MEMS beam is plotted as a function of $\varepsilon/\varepsilon_{\mathrm{cr}}$ in Fig. 1(c) with various x_{T}/h. When x_0=0, ε_{r} increases with ε in a one-to-one ratio until $\varepsilon=\varepsilon_{\mathrm{cr}}$, and then ε_{r} remains at $\varepsilon_{\mathrm{cr}}$ instead of continuing to increase with ε. On the other hand, when x_0>0, ε_r increases with ε but never reaches $\varepsilon_{\mathrm{cr}}$. This is because the increased center deflection from x_0 to x_{T} releases part of the compressive strain, thus, ε_{r} is always smaller than ε and $\varepsilon_{\mathrm{cr}}$ when x_0>0.

Furthermore, the increased center deflection changes the resonance frequency of the MEMS resonator. Fig. 1(d) shows the normalized resonance frequency, f/f_0, as a function of $\varepsilon/\varepsilon_{\mathrm{cr}}$ calculated for various x_0/h. When x_0/h =0, the frequency drops to zero at $\varepsilon/\varepsilon_{\mathrm{cr}}=1$ and then increases from zero to higher values because the MEMS beam enters the buckling regime [29]. When x_0/h>0, the frequency levels off instead of dropping to zero, and the steep frequency change also gradually disappears as x_0 increases, which is not conducive to achieving high sensitivity [15]. Please note that as x_0 increases, the lowest resonance frequency that can be achieved by strain tuning increases, and the buckling point shifts to a lower strain ($\varepsilon/\varepsilon_{cr}$ <1) as indicated by the marks in Fig. 1 (d). Here, we define the point where the frequency polarity changes in each curve as the buckling point (buckling condition), and its corresponding strain is called buckling strain. As shown in Fig. 1(d), the buckling strains for x_0/h =0-0.20 are $\varepsilon/\varepsilon_{cr}$ =1, 0.85, 0.72, 0.65, 0.59 respectively.

From Eq. (11), we know that the cubic nonlinearity coefficient α is not affected by the compressive strain, but the quadratic nonlinearity coefficient β is proportional to x_T. We therefor plotted the calculated β as a function of $\varepsilon/\varepsilon_c$ on the right y-axis of Fig. 1(b). As seen, for the cases x_0>0, β generally increases with increased compressive strain, and the increase in β becomes steeper when the value of $\varepsilon/\varepsilon_{cr}$ approaches the buckling strain. Since β gives a softening nonlinearity, such a steep increase in the quadratic (softening) nonlinearity is expected to dramatically compensate for the cubic (hardening) nonlinearity, resulting in modulating the total nonlinearity significantly.

To show the strain tuning effect on the suppression of frequency shift, here, we take the case of the initial center deflection x_0/h =0.1 as an example. Regarding other cases of the initial center deflection, please see the supplementary material. Figure 2 plots the normalized resonance frequency, f/f_0, as a function of the oscillation amplitude, calculated for various $\varepsilon/\varepsilon_{cr}$ in the case of x_0/h =0.1. As seen, when the compressive strain is small, the resonance frequency shifts to a higher frequency side with increasing oscillation amplitude and the nonlinearity does not change significantly, indicating that the hardening cubic nonlinearity dominates the total nonlinearity. However, as the compressive strain approaches the buckling strain ($\varepsilon/\varepsilon_{cr}$ =0.72), the positive frequency shift reduces significantly owing to the enhanced quadratic softening nonlinearity and the frequency shift reaches a minimum at $\varepsilon/\varepsilon_{cr}$ =0.66. When the compressive strain exceeds the $\varepsilon/\varepsilon_{cr}$ =0.66, the resonance frequency shifts to the lower frequency side, indicating that the total nonlinearity has been tuned to softening under this condition. We therefore conclude that the nonlinearity of the MEMS beam can be well suppressed by approaching the buckling condition of the MEMS beam.

In addition, we also found that, although the nonlinearity can be controlled by increasing x_0 without applying the compressive strain, a large x_0 will reduce the responsivity of the MEMS resonator (See the supplementary material for more details [30]), which is not preferable for high-sensitivity sensing applications [15]. Thus, in this work, we have tried to suppress x_0 to be a very small value (x_0/h = ~0.01), for achieving both a large responsivity and a small nonlinearity by approaching the buckling condition.

Experimental setup and results

Electrothermal effect [20] and lattice mismatch [21] have been proposed to induce strain in MEMS beam resonators. Since the electrothermal effect may induce some additional noise during the heating, we demonstrate the nonlinearity control of MEMS beam resonators using the compressive strain induced by lattice mismatch in this work. We grew an $In_xGa_{1-x}As$/AlGaAs heterostructure on a GaAs substrate, whose structure is schematically shown in Fig. 3(a). Owing to the lattice mismatch between InAs and GaAs, there is a compressive strain preloaded in the $In_xGa_{1-x}As$ layer, given by [21]

$$\varepsilon_l = \left(\frac{a_{\mathrm{InAs}}}{a_{\mathrm{GaAs}}} - 1\right) x \qquad (14),$$

where α_{InAs} and α_{GaAs} are the lattice constants of InAs and GaAs, respectively, and x represents the content of indium in $In_xGa_{1-x}As$. After growing a 100-nm-thick GaAs buffer layer and a 2-µm-thick $Al_{0.7}Ga_{0.3}As$ sacrificial layer on a GaAs substrate, the beam layer was formed by depositing a GaAs/$Al_{0.3}Ga_{0.7}As$ superlattice buffer layer and a 1-µm-thick $In_{0.004}Ga_{0.996}As$ layer. Here, the superlattice buffer layer is used to ensure a homogenous growth of the beam layer in the wafer growth by MBE [31]. Then, we formed a 2-dimensional electron gas (2DEG) layer by growing an 80-nm-thick $n^+Al_{0.3}Ga_{0.7}As$ layer and a 10-nm-thick undoped GaAs capping layer. Fig. 3 (b) shows the schematic structure of the fabricated doubly clamped MEMS beam. The suspended beam is formed by selectively etching the sacrificial layer with diluted hydrofluoric acid (HF). The mesa layer and 2 top NiCr gates (12 nm) on both ends of the beam form two piezoelectric capacitors C_1 and C_2 together with the 2DEG layer. A microscope image of the MEMS resonators is shown in Fig. 3(c). We drove the beam into oscillation by applying an ac voltage (V_D) to one of the piezoelectric capacitors and then measured the beam oscillation by a laser Doppler vibrometer and a lock-in amplifier with a built-in phase locked loop (PLL). In addition, we deposited a 12-nm-thick NiCr layer on the middle part of the beam as a heater for calibrating the thermal response. All the measurements were performed in a vacuum (~10^{-4} Torr) at room temperature.

Since the nonlinearity is expected to be significantly modulated near the buckling point of the MEMS beam and the buckling point is close to $\varepsilon/\varepsilon_{cr}$=1 for a small x_0 [see Fig. 1(d)], the lattice-mismatch strain ε_l must be close to the ε_{cr}. However, it is difficult to grow many $In_xGa_{1-x}As$ wafers with various indium concentrations. Since the ε_{cr} is a function of beam length, L, ($\varepsilon_{cr} = \frac{\pi^2}{3}\frac{h^2}{L^2}$), in this work, we realized the buckling condition by varying the length of the MEMS beams to make ε_{cr} approach the fixed ε_l and thus modulated the nonlinearity. We fabricated $In_{0.004}Ga_{0.996}As$ MEMS beam resonators with various beam lengths, L=51~111 μm, and measured the resonance frequency with a driving voltage V_D = 20 mV. Fig. 4(a) shows the resonance frequency (lines: theoretical calculation, dots: experimental results) of the $In_{0.004}Ga_{0.996}As$ beams as a function of L. As seen, the measured resonance frequency reasonably agrees with that of theoretical calculation at x_0/h =0.01, indicating that the initial center deflection is ~10 nm for the present MEMS beam resonators, which may come from the plastic deformation during the fabrication process. Furthermore, the frequency polarity changes at L=103 μm, which is regarded as the buckling point, and a small nonlinearity (i.e., small resonance frequency shift) is expected to be observed near this point.

To estimate the mechanical nonlinearity of the MEMS beams and compare it with the theoretical calculation result, we have driven the MEMS resonator at different amplitudes and measured the resonance frequencies (f). The MEMS resonator has been driven at a self-sustained oscillation mode at various driving voltages (V_D=10-400 mV) by using a PLL. Fig. 4(b) plots the calculated resonance frequency shift ($\Delta f=f-f_0$) as a function of oscillation amplitude at various L (97-105 μm). As seen in Fig. 4(b), for a small oscillation amplitude (~100 nm), with the beam length varying from 97 to 105 μm, Δf first reduces and reaches a minimum at L=101 μm, and then shifts to the negative side, indicating that the nonlinearity has been tuned from hardening to softening. However, at the large oscillation amplitude range (>~200nm), the resonance frequencies of L>101μm shift to the higher frequency again. This result indicates that the nonlinearity at small amplitudes is softening but hardening at large amplitudes, which can be understood by the fact that the hardening nonlinearity is cubic, but the softening nonlinearity is quadratic. Since the orders of the two nonlinearities are different, the total nonlinearity depends on the oscillation amplitude.

Fig. 4(c) shows the measured resonance frequency shift (Δf) of $In_{0.004}Ga_{0.996}As$ samples as a function of the oscillation amplitude with various L. As seen, the Δf changes from positive to negative as the beam length increases, indicating the nonlinearity is tuned from hardening to softening. For a small oscillation amplitude range (0-100nm), Δf reaches a minimum at L=101 μm, which is consistent with the theoretical calculation in Fig. 4(b). Moreover, the Δf does not change significantly from L=51 μm to L=97 μm but is rapidly tuned near the buckling point. This is because the increase in the quadratic nonlinearity coefficient β becomes steeper near the buckling condition. The above results demonstrate that the MEMS resonator exhibits a small nonlinearity by approaching the buckling condition of the MEMS beam.

It has been found that the calculated Δf agrees with the experimental data nicely for small and moderate amplitude ranges (0-200 nm). However, at larger amplitudes (>200nm), there is a notable discrepancy between calculated Δf (Fig. 4(b)) and measurement data (Fig. 4(c)). Such a discrepancy may be owing to the fluctuation of the beam lengths (L). In the Fig. 4 (c), the beam length L is a designed value. The actual beam length, however, may be slightly shorter or longer owing to the random fabrication errors, which gives the different experimental Δf with the calculation results. Furthermore, the theoretical model shown in this research is based on an approximation of the cubic nonlinearity of the MEMS beam (see Eq. (4) in Ref. [23]). However, the higher-order nonlinearities (e.g., 5th, 7th…) also exist and may contribute to the discrepancies between experiment and calculation at very large oscillation amplitudes. Nevertheless, the trend of the nonlinearity change with beam lengths has been well shown in both numerical and experimental results.

At a large oscillation amplitude, the polarity change of Δf predicated by the numerical result has been observed. Fig. 4(d) plots a blow-up of the measured Δf-amplitude curve for the MEMS beam with L=103 μm, together with the numerical Δf- amplitude curve for L=104 μm, where the resonance frequency first decreases at small amplitudes but levels off and then increases at large amplitudes, as indicated by the red arrows. As seen, the experimental result for L=103 μm shows a good agreement with the numerical result for L=104 μm, indicating that the actual beam length of this sample is probably closer to 104 μm rather than the designed 103 μm. It should be noted that the boundary condition where the nonlinearity changes the polarity (shown by the red dot in Fig. 4(d)) is given a zero-dispersion point [32,33], where the resonance frequency is locally independent of the amplitude ($d\omega/dE$=0). Thus, at this point, the amplitude fluctuation does not induce additional frequency noise, which is similar to the linear oscillation regime, but its oscillation amplitude is much larger than the linear oscillation amplitude without the preloaded lattice-mismatch strain. Therefore, the zero-dispersion point is very promising for low-noise sensing applications.

To intuitively show the effect of α and β on the total nonlinearity (Y_T) of MEMS beam, we estimated the Y_T by fitting the equation described in Ref. [34],

$$f = f_0(1 + Y_T A^2) \tag{15}$$

Where f and f_0 are the measured resonance frequency and the natural resonance frequency without oscillation, respectively, and A is the oscillation amplitude. The fitting was performed at a small oscillation amplitude range of approximately 0-50 nm, with the data shown in Fig. 4(c). The result is shown by the dots in Fig. 5(a). As seen, Y_T keeps a stable value when the beam length is small(L<~100μm), and quickly drops to a negative value when approaching the buckling condition (L=103μm). When L exceeds ~108μm, Y_T rises from the negative value ($|Y_T|$ decreases).

To understand the origin of the nonlinearity change, we have calculated the effective nonlinearity, $Y_{(\alpha,\beta)}$, by using the cubic (α) and quadratic (β) nonlinearity coefficients and, following the equation described in Ref. [35],

$$Y_{(\alpha,\beta)} = \frac{3}{8}\frac{\alpha}{\omega_0^2} - \frac{5}{12}\frac{\beta^2}{\omega_0^4} \tag{16}$$

Where $\omega_0=2\pi f_0$. In addition, to quantitatively understand how α and β affect the effective nonlinearity, we also calculated $Y_{(\alpha)} = \frac{3}{8}\frac{\alpha}{\omega_0^2}$ and $Y_{(\beta)} = -\frac{5}{12}\frac{\beta^2}{\omega_0^4}$. The calculated $Y_{(\alpha,\beta)}$, $Y_{(\alpha)}$ and $Y_{(\alpha,\beta)}$ are shown by the black, blue and red curves in Fig. 5(a). The α and β used for this calculation are shown as the solid and dashed curves in Fig. 5(b). As seen in Fig. 5(a), the calculated $Y_{(\alpha,\beta)}$ reasonably agrees with the experimental Y_T. When L is small ($L < 100$ um), $Y_{(\alpha,\beta)}$ and $Y_{(\alpha)}$ have the same trace, indicating the nonlinearity is dominated by the α term under this condition. The MEMS beam thus exhibits hardening nonlinearity. Furthermore, we can see that $Y_{(\alpha)}$ does not change much with the increasing L before reaching the buckling condition. This is because, although α decreases with L as shown in Fig.5 (b), ω_0 also decreases with L (see Fig. 4(a)), giving a stable $Y_{(\alpha)}$ and furthermore a stable $Y_{(\alpha,\beta)}$ (β is very small in this case). However, $Y_{(\alpha,\beta)}$ changes its trend to be the same as $Y_{(\beta)}$ when approaching the buckling condition, indicating the nonlinearity is dominated by the β term from then. As a result, $Y_{(\alpha,\beta)}$ quickly drops to a negative value owing to the large increase in β (see Fig.5 (b)), a quasi-zero nonlinearity is thereby achieved near the buckling condition. Moreover, there is a reversal of polarity in $Y_{(\alpha,\beta)}$ when L exceeds ~105μm, which is because the ω_0 starts to increase with the further increase in L [(see Fig. 4(a)].

Note that there is a small difference in the lengths where Y_T and $Y_{(\alpha,\beta)}$ achieve the minimum value. This is probably because the experimental beam lengths may be slightly different from the designed values, or the control of indium composition was not perfect (x in $In_xGa_{1-x}As$) in the wafer growth, and the buckling condition is very sensitive to the beam length and actual x. However, the main feature of the experimental nonlinearity (Y_T) has been well reproduced by the numerical calculated nonlinearity ($Y_{(\alpha,\beta)}$).

Conclusion

In summary, we have clarified the mechanism of strain tuning effect on the mechanical nonlinearity in doubly clamped GaAs MEMS beam resonators and demonstrated that the mechanical nonlinearity can be greatly suppressed by preloading a lattice-mismatch strain in the MEMS beam. The nonlinearity of the MEMS beam arises from the hardening and softening nonlinearity terms in the Duffing equation. By approaching the buckling condition of the MEMS beam, the softening nonlinearity greatly compensates for the hardening nonlinearity, and the total nonlinearity is thus suppressed. Utilizing this knowledge, we fabricated $In_xGa_{1-x}As$ MEMS beams working near the buckling condition and measured the frequency shift as a function of oscillation amplitude. As a result, the frequency shift of the MEMS resonator is well suppressed near the buckling condition, and a zero-dispersion operation point has been achieved, which is very promising for low-noise sensing applications with MEMS resonators. The demonstrated approach provides a promising path to suppress the nonlinearity of the MEMS beam and enables the low-noise operation of MEMS resonators. Furthermore, the use of effective nonlinearity to reproduce the total nonlinearity intuitively shows the effect of hardening and softening nonlinearities on the total nonlinearity, allowing one can understand the origin of the nonlinearity change.

Acknowledgments

This work has been partly supported by the A-STEP program of JST, MEXT Grant-in-Aid for Scientific Research on Innovative Areas “Science of hybrid quantum systems” (15H05868), and KAKENHI from JSPS (21K04151).

References

[1] K. Ekinci and M. Roukes, Nanoelectromechanical systems, Rev. Sci. Instrum. 76, 061101 (2005).

[2] A. Boisen, S. Dohn, S. S. Keller, S. Schmid, and M. Tenje, Cantilever-like micromechanical sensors, Rep. Prog. Phys.74(3), 036101 (2011).

[3] A. N. Cleland, Foundations of Nanomechanics: From Solid-State Theory to Device Applications (Springer Science & Business Media, 2013).

[4] K. L. Ekinci, X. M. H. Huang, and M. L. Roukes, Ultrasensitive nanoelectromechanical mass detection, Appl. Phys. Lett. 84, 4469 (2004).

[5] S. Dohn, R. Sandberg, W. Svendsen, and A. Boisen, Enhanced functionality of cantilever based mass sensors using higher modes, Appl. Phys. Lett. 86, 233501 (2005).

[6] K. Jensen, K. Kim, and A. Zettl, An atomic-resolution nanomechanical mass sensor, Nat. Nanotechnol. 3, 533 (2008).

[7] D. Rugar, R. Budakian, H. Mamin, and B. Chui, Single spin detection by magnetic resonance force microscopy, Nature. 430, 329 (2004).

[8] A. N. Cleland and M. L. Roukes, A nanometre-scale mechanical electrometer, Nature. 392, 160 (1998).

[9] R. Knobel, C. S. Yung, and A. N. Cleland, Single-electron transistor as a radio-frequency mixer, Appl. Phys. Lett. 81, 532 (2002).

[10] X. Wang, X. Wei, D. Pu, and R. Huan, Single-electron detection utilizing coupled nonlinear microresonators, Microsyst Nanoeng. 6, 78 (2020).

[11] A. K. Pandey, O. Gottlieb, O. Shtempluck, and E. Buks, Performance of an AuPd micromechanical resonator as a temperature sensor, Appl. Phys. Lett. 96, 203105 (2010).

[12] T. Larsen, S. Schmid, L. Grönberg, A. Niskanen, Ultrasensitive string-based temperature sensors, J. Hassel, S. Dohn, and A. Boisen, Appl. Phys. Lett. 98, 121901 (2011).

[13] A. Svetlitza, T. Blank, S. Stolyarova, I. Brouk, S. B. L. Shefi, and Y. Nemirovsky, CMOS-

SOI-MEMS thermal antenna and sensor for uncooled THz imaging, IEEE Transactions on Electron Devices. 63(3), 1260 (2016).

[14] X. C. Zhang, E. B. Myers, J. E. Sader, and M. L. Roukes, Nanomechanical torsional resonators for frequency-shift infrared thermal sensing, Nano Lett. 13, 1528 (2013).

[15] Y. Zhang, Y. Watanabe, S. Hosono, N. Nagai, and K. Hirakawa, Room temperature, very sensitive thermometer using a doubly clamped microelectromechanical beam resonator for bolometer applications, Appl. Phys. Lett.108 (16), 163503 (2016).

[16] Y. Zhang, S. Hosono, N. Nagai, S.-H. Song, and K. Hirakawa, Fast and sensitive bolometric terahertz detection at room temperature through thermomechanical transduction, J. Appl. Phys. 125, 151602 (2019).

[17] T. Fukuma, M. Kimura, K. Kobayashi, K. Matsushige, and H. Yamada, Development of low noise cantilever deflection sensor for multienvironment frequency-modulation atomic force microscopy, Rev. Sci. Instrum. 76, 053704 (2005).

[18] D. Antonio, D. H. Zanette, and D. López, Frequency stabilization in nonlinear micromechanical oscillators, Nat. Commun. 3, 806 (2012).

[19] Y. Zhang, Y. Yoshioka, I. Morohashi, and X. Liu, 1: 1 internal mode coupling strength in GaAs doubly-clamped MEMS beam resonators with linear and nonlinear oscillations, Appl. Phys. Express 14, 014001 (2021).

[20] Y. Zhang, Y. Yoshioka, M. Iimori, B. Qiu, X. Liu, and K. Hirakawa, Thermal tuning of mechanical nonlinearity in GaAs doubly-clamped MEMS beam resonators, Applied Physics Letters. 119 (16), (2021).

[21] B. Qiu, Y. Zhang, N. Nagai, and K. Hirakawa, Enhancing the thermal responsivity of microelectromechanical system beam resonators by preloading a critical buckling strain, Applied Physics Letters. 119 (15), (2021).

[22] Mohammad I Younis, MEMS linear and nonlinear statics and dynamics (Springer Science & Business Media, 2011).

[23] Lifshitz, Ron, and Michael C. Cross, Nonlinear dynamics of nanomechanical and micromechanical resonators (Reviews of nonlinear dynamics and complexity 1.1, 2008).

[24] F. Tajaddodianfar, M. R. H. Yazdi, and H. N. Pishkenari, Nonlinear dynamics of MEMS/NEMS resonators: analytical solution by the homotopy analysis method, Microsystem Technologies. 23 (6), 1913-1926, (2017).

[25] A. Z. Hajjaj, M. A. Hafiz, and M. I. Younis, Mode coupling and nonlinear resonances of MEMS arch resonators for bandpass filters, Sci Rep. 7, 41820 (2017).

[26] F. Tajaddodianfar, M. R. H. Yazdi, H. N. Pishkenari, and E. M. Miandoab, Nonlinear dynamics of electrostatically actuated micro-resonator: analytical solution by homotopy perturbation method, in 2014 IEEE/ASME International Conference on Advanced Intelligent Mechatronics (pp. 1284-1289), IEEE.

[27] S. Neumeyer, V. S. Sorokin, and J. J. Thomsen, Effects of quadratic and cubic nonlinearities on a perfectly tuned parametric amplifier, Journal of Sound and Vibration. 386, 327 (2017).

[28] S. A. Tella, A. Z. Hajjaj, and M. I. Younis, Special Section on the Dynamics of MEMS and NEMS, Journal of Vibration and Acoustics. 139 (4) (2017).

[29] A. Z. Hajjaj, N. Alcheikh, A. Ramini, M. A. Al Hafiz, and M. I. Younis, Highly tunable electrothermally and electrostatically actuated resonators, Journal of Microelectromechanical Systems. 25 (3), 440 (2016).

[30] See Supplemental Material at [URL] for more details about the effect of initial center deflection and compressive strain on nonlinearity and responsivity.

[31] I. Mahboob and H. Yamaguchi, Bit storage and bit flip operations in an electromechanical oscillator, Nat. Nanotechnol. 3, 275 (2008).

[32] S. Rosenberg and O. Shoshani, Zero-dispersion point in curved micro-mechanical beams, Nonlinear Dynamics. 107 (1), 1 (2021).

[33] L. Huang, S. Soskin, I. Khovanov, R. Mannella, K. Ninios, and H. B. Chan, Frequency stabilization and noise-induced spectral narrowing in resonators with zero dispersion, Nat. Commun. 10, 3930 (2019).

[34] L. L. Li, P. M. Polunin, S. Dou, O. Shoshani, B. S. Strachan, J. S. Jensen, S.W. Shaw and K. L. Turner, Tailoring the nonlinear response of MEMS resonators using shape optimization, Applied Physics Letters, 110(8), 081902 (2017).

[35] S. Dou, B. S. Strachan, S. W. Shaw, and J. S. Jensen, Structural optimization for nonlinear dynamic response, Philos Trans A Math Phys Eng Sci. 373, (2051) (2015).

Figure Captions

Figure 1 (a) Schematic diagram of a MEMS beam with an initial center deflection in the steady-state and oscillatory state. When the center deflection increases from x_0 to x_T, the MEMS beam has a new equilibrium position for the oscillation. (b) The calculated center deflection x_T/h, (left y-axis) and quadratic nonlinearity coefficient β (right y-axis) as a function of the compressive strain ($\varepsilon/\varepsilon_{cr}$) at various initial center deflections (x_0/h=0, 0.05, 0.1, 0.15, 0.2). x_0 and x_T are normalized by the thickness (h) of the MEMS beam, and ε is normalized by the buckling critical strain ε_{cr} of the MEMS beam. This figure is adapted from Fig. 2(b) of Ref. [20]. (c) The calculated residual strain ($\varepsilon_r/\varepsilon_{cr}$) as a function of the compressive strain ($\varepsilon/\varepsilon_{cr}$) at various initial center deflections. (d) The calculated resonance frequency (f/f_0) as a function of $\varepsilon/\varepsilon_{cr}$ at various initial center deflections, the frequency is normalized by the natural frequency (f_0) without ε. The buckling points are marked by geometric shapes of different colors. This figure is adapted from Fig. 2(a) of Ref. [20].

Figure 2 The calculated resonance frequency (f/f_0) as a function of oscillation amplitude at various $\varepsilon/\varepsilon_{cr}$ values; the initial center deflection is x_0/h = 0.1. The frequency is normalized by the natural frequency f_0 without oscillation.

Figure 3 (a) The wafer structure used for fabricating the $In_{0.004}Ga_{0.996}As$ MEMS beam resonators. (b) Schematic structure of the fabricated doubly clamped MEMS beam. The mesa layer and 2 top gates (NiCr = 12 nm) on both ends of the beam form two piezoelectric capacitors, C_1 and C_2 together with the 2DEG layer. A 12-nm-thick NiCr layer was deposited as a heater for calibrating the thermal response. (c) A microscope image of fabricated MEMS beam resonator. An ac voltage is applied to one of the piezoelectric capacitors to drive the resonator and the induced mechanical oscillation is measured by a laser Doppler vibrometer and a lock-in amplifier with a built-in PLL.

Figure 4 (a) The resonance frequency (line: theoretical calculation, dot: experimental results) of the $In_{0.004}Ga_{0.996}As$ beams as a function of L. (b) The calculated resonance frequency shifts (Δf) as a function of oscillation amplitude at various L (97-105 μm). (c) The measured resonance frequency shifts (Δf) of $In_{0.004}Ga_{0.996}As$ samples with various L. (d) A blow-up of the measured Δf-amplitude curve for the MEMS beam with L=103 μm (dots), together with the numerical Δf-a curves for L=104 μm (line). The red arrows show the change in resonant frequency. At the zero-dispersion point (red dot), there is an extremum of the frequency with a zero slope, and hence, the frequency is locally independent of the amplitude.

Figure 5 (a) The estimated total nonlinearity, Y_T, and the calculated effective nonlinearity coefficient, $Y_{(\alpha,\beta)}$, as well as its two terms $Y_{(\alpha)}$ and $Y_{(\beta)}$ as a function of L. Y_T is estimated by the linear fitting, using the data at an oscillation amplitude range of approximately 0-50 nm in Fig. 4 (c). (b) The calculated cubic nonlinearity coefficient α and quadratic nonlinearity coefficient β as a function of L.

Figures

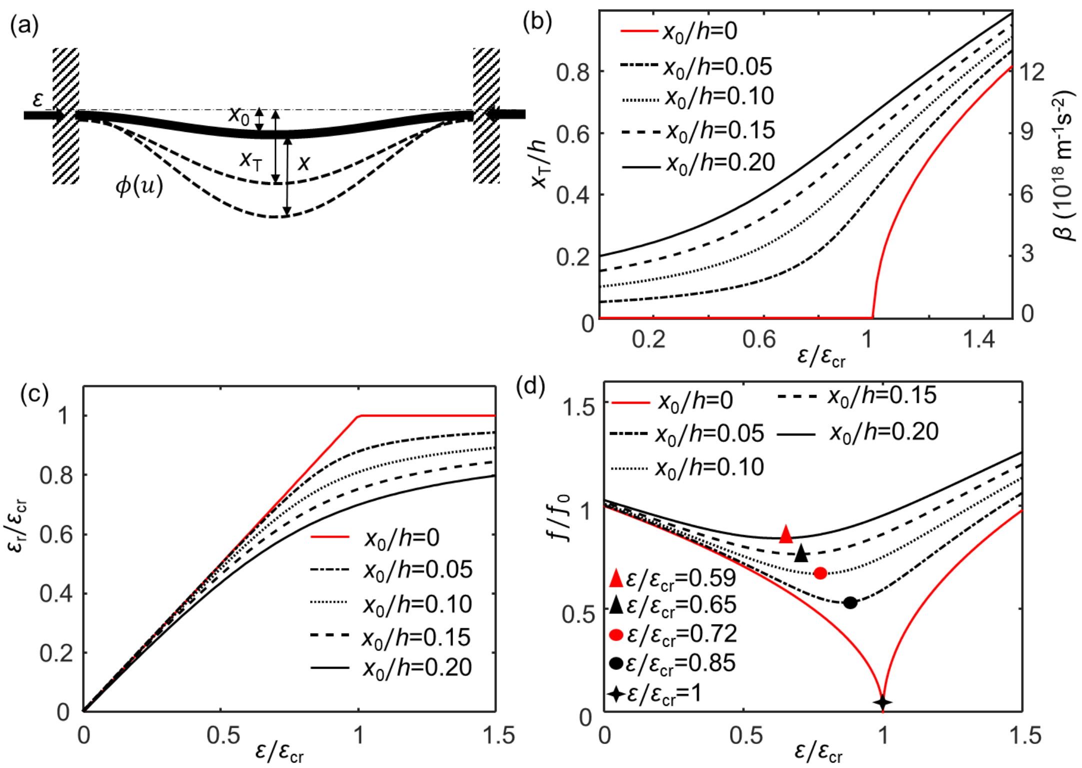

Fig. 1

Li Chao, et al.

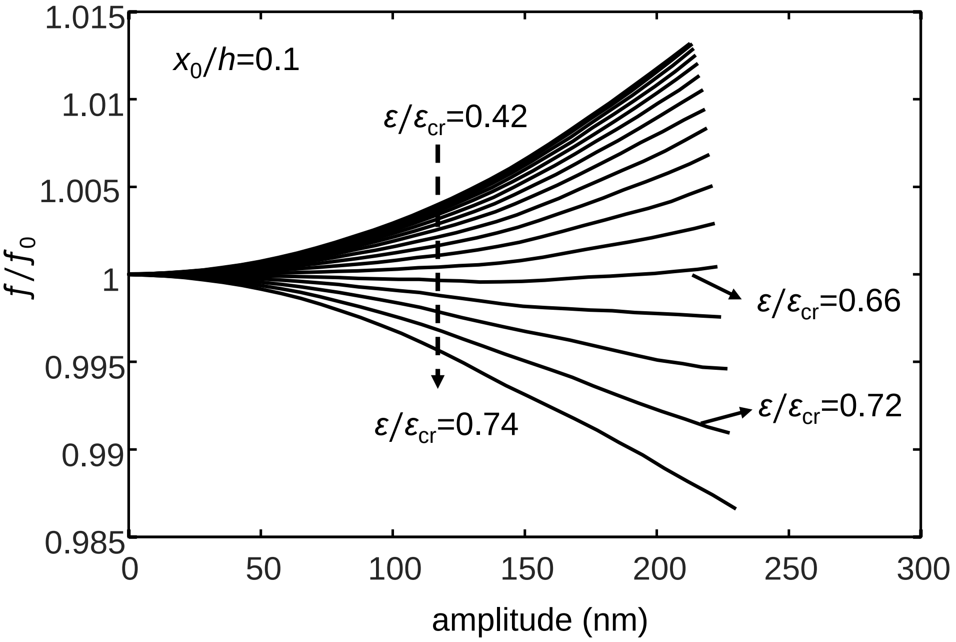

Fig. 2

Li Chao, et al.

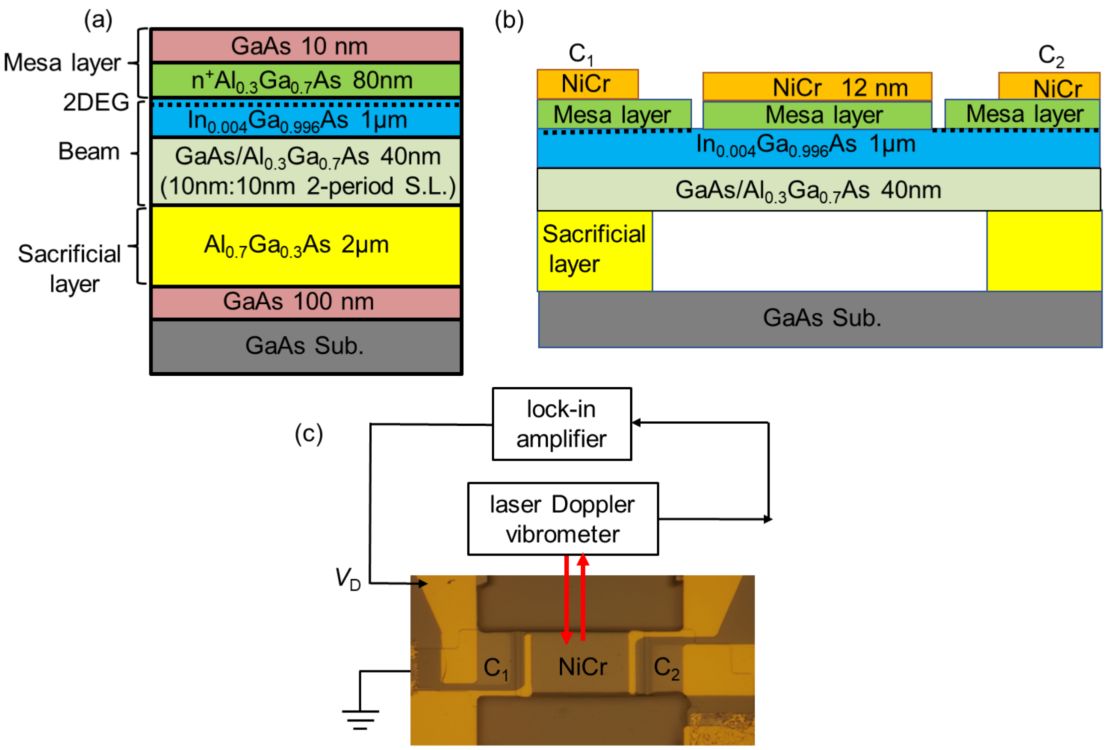

Fig. 3

Li Chao, et al.

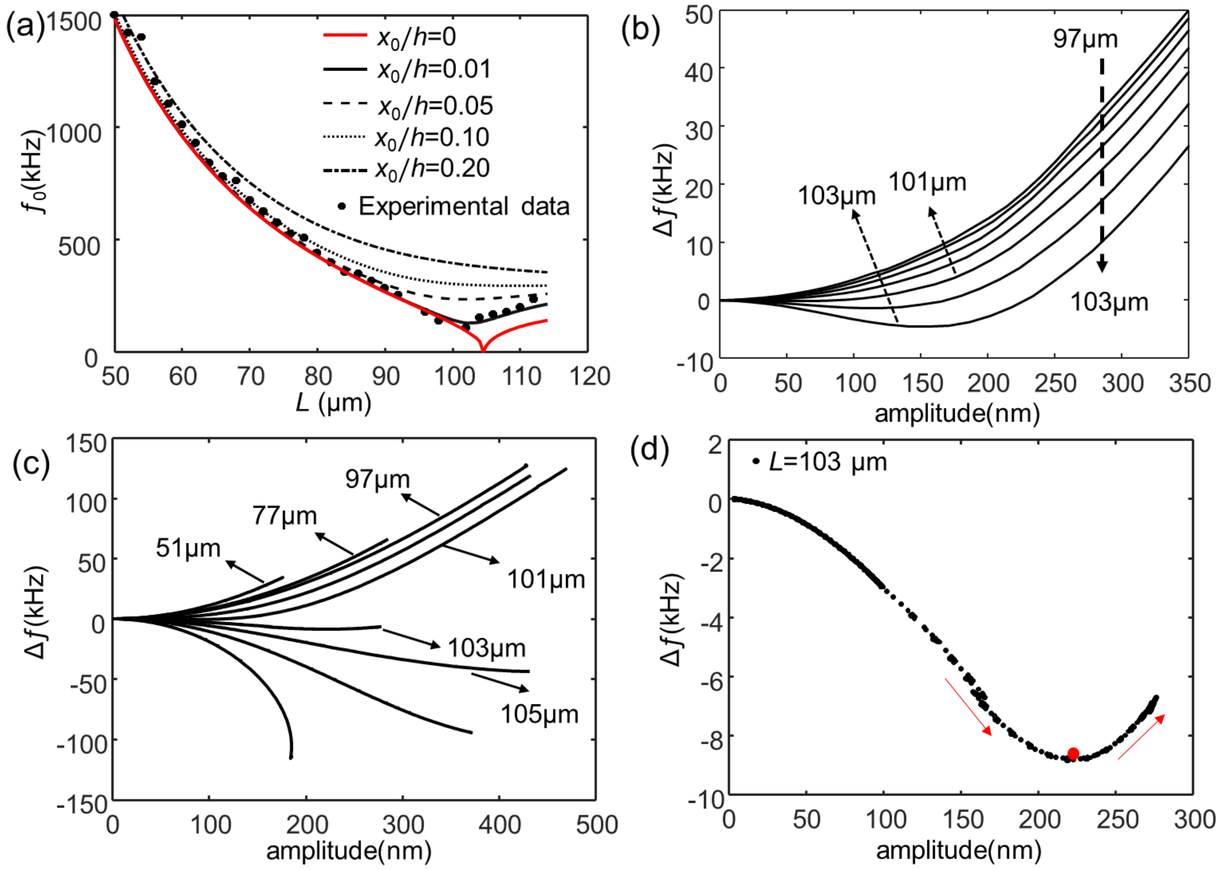

Fig. 4

Li Chao, et al.

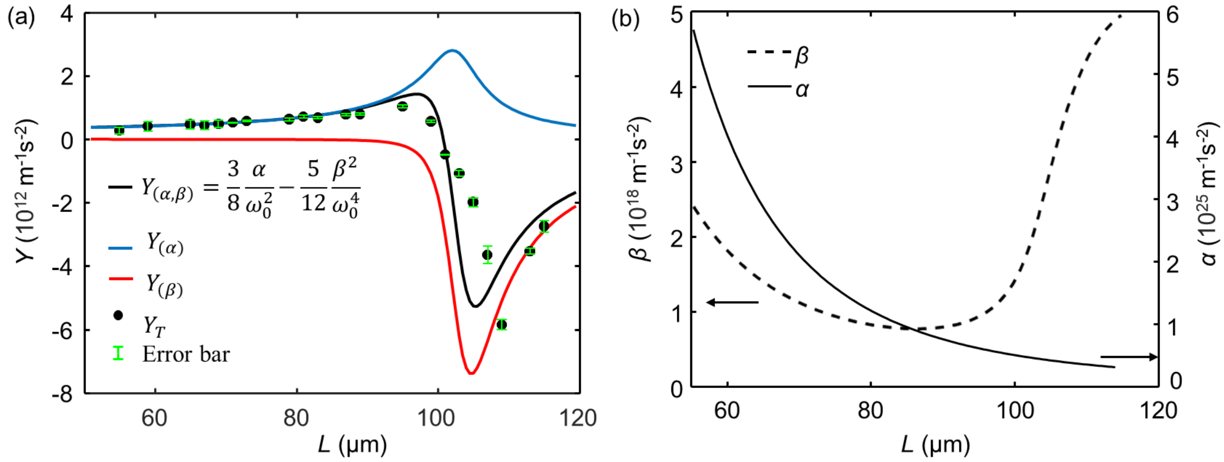

Fig. 5

Li Chao, et al.